A MERMAID Miscellany: Seismoacoustic Signals beyond the *P* Wave

Joel D. Simon*[1], Frederik J. Simons[1], and Jessica C. E. Irving[2]

Abstract

Mobile Earthquake Recorder in Marine Areas by Independent Divers (MERMAID) is a passively drifting oceanic diving float that transmits acoustic pressure records from global earthquakes within hours or days of their rupture. The onboard algorithm used for the detection and identification of signals from the hydrophone prioritizes the recovery of ∼1 Hz teleseismic *P* waves, which are useful for seismic imaging of Earth's mantle. Two years into a mission that launched 50 MERMAIDs to map 3D mantle wavespeed anomalies with high resolution under the Pacific in French Polynesia, it is clear that the data returned contain much information beyond the first-arriving seismic *P* phases. These include acoustic conversions from *S* waves, surface waves, *T* waves, and inner- and outer-core phases, generated by earthquakes heard across the globe—and sounds from otherwise unidentified events occurring in remote and uninstrumented parts of the world's oceans. Our growing database of automatically accumulating ∼240 s long-triggered segments contains a treasure trove for geophysicists interested in seismology beyond *P*-wave tomography. Furthermore, equipped with two-way communication capabilities, MERMAID can entertain requests to deliver data from its 1 yr buffer. In this article, we highlight the data classes and categories in MERMAID's "extended-utility" catalog.

Cite this article as Simon, J. D., F. J. Simons, and J. C. E. Irving (2021). A MERMAID Miscellany: Seismoacoustic Signals beyond the *P* Wave, *Seismol. Res. Lett.* **92**, 3657–3667, doi: 10.1785/0220210052.

Introduction

We present an overview of the diverse signals beyond teleseismic *P* waves recorded by Mobile Earthquake Recorder in Marine Areas by Independent Divers (MERMAID). MERMAID is a freely drifting hydrophone that records earthquakes within the world's oceans. It periodically surfaces at its own discretion to update its location and correct instrumental clock-drift errors via its built-in Global Positioning System receiver and to transmit waveforms in near real-time via the commercial Iridium satellite constellation. MERMAID was designed to return teleseismic tomographic-quality ∼1 Hz *P*-wave arrivals (Sukhovich *et al.*, 2011, 2014), and the first-generation (Simons *et al.*, 2006, 2009) and second-generation floats (Hello *et al.*, 2011; Joubert *et al.*, 2016) have been shown to do this quite well (Sukhovich *et al.*, 2015; Nolet *et al.*, 2019; Simon *et al.*, 2020).

The signals shown in this study were recorded by the commercially available third-generation MERMAID version designed by Yann Hello at Géoazur and manufactured by French underwater engineering firm OSEAN SAS (Hello and Nolet, 2020). This latest MERMAID model has a lifetime of 5 yr, and 46 out of 50 instruments initially deployed are currently active and reporting data around French Polynesia in the South Pacific. All signals presented here were recorded during the ongoing South Pacific Plume Imaging and Modeling (SPPIM) project overseen by the international EarthScope-Oceans consortium. For a near real-time map of the entire SPPIM array, including downloadable historical drift-trajectory data, see Data and Resources. In this study, we only consider the data returned by the 16 floats owned and maintained by Princeton University. Their surface locations over 16 months of deployment are plotted as colorful drift tracks in Figure 1. (MERMAID 23 was recovered and redeployed, which explains the gap in the drift track, and MERMAID numbers 14 and 15 never existed.)

Earthquake identification and *P*-wave travel-time residual determination, and their uncertainties, for incorporation into tomographic models of the plume-rich region of interest, are ongoing following the procedures outlined by Simon *et al.* (2020). The present study complements a separate analysis by the authors (J. D. Simon *et al.*, unpublished manuscript, 2021, see Data and Resources), which is a singular look at MERMAID's primary target: mantle *P* waves of tomographic quality. There, readers will find an exhaustive discussion of

1. Department of Geosciences, Princeton University, Princeton, New Jersey, U.S.A., https://orcid.org/0000-0003-2444-0564 (JDS); https://orcid.org/0000-0003-2021-6645 (FJS); 2. School of Earth Sciences, University of Bristol, Bristol, United Kingdom, https://orcid.org/0000-0002-0866-8246 (JCEI)

*Corresponding author: jdsimon@alumni.princeton.edu

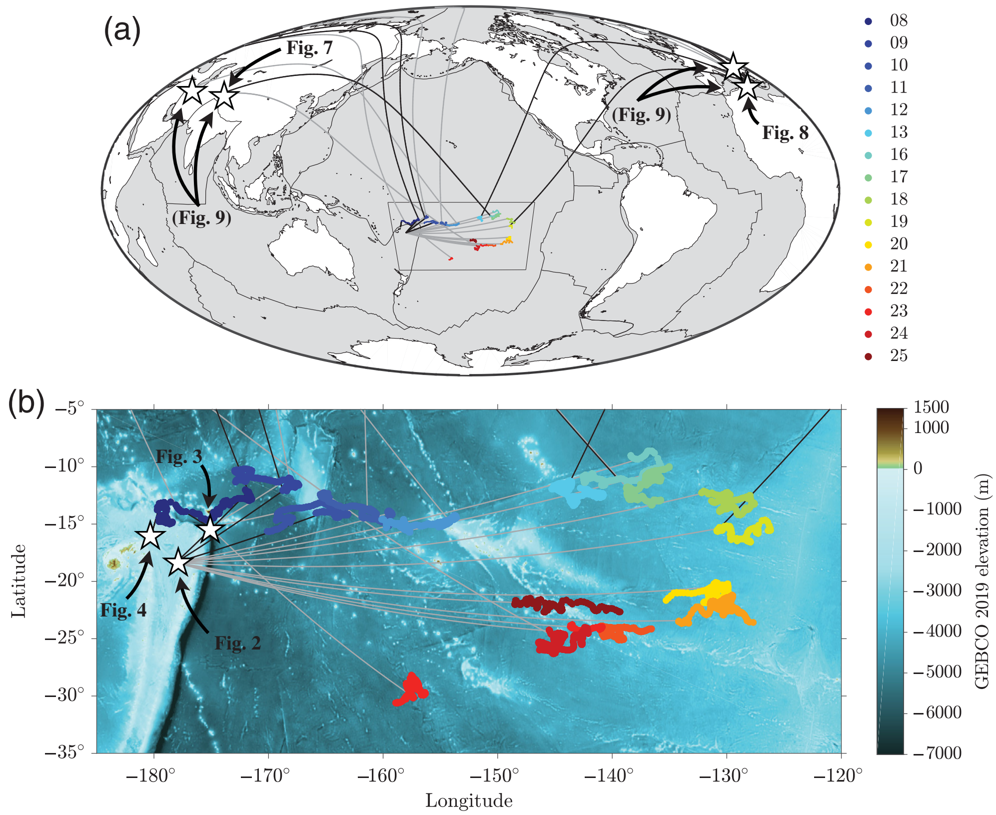

Figure 1. Ray paths connecting earthquake epicenters and interpolated Mobile Earthquake Recorder in Marine Areas by Independent Divers (MERMAID) locations at the time of recording the seismograms shown in this study. (a) Global map with legend noting the unique portion of MERMAID serial numbers. The box in the South Pacific marks the boundaries of the regional map in panel (b). (b) South Pacific Plume Imaging and Modeling (SPPIM) project-array drift tracks from deployment between August and September of 2018 to the end of 2019 in the same color scheme as panel (a), overlain on a map of bathymetry and topography (General Bathymetric Chart of the Oceans [GEBCO] Bathymetric Compilation Group, 2019). In both maps, arrows pointing to earthquake epicenters identify the figure numbers in which their seismograms (or travel-time residual data when the reference appears within parentheses) appear in this article. Ray paths associated with seismograms actually shown in this article are colored black.

MERMAID's data quality compared with traditional seismometers and Raspberry Shake sensors installed on nearby islands, as well as a discussion of MERMAID's seismic catalog, its completeness, and rate-of-data-return statistics compared against historical ocean-bottom seismometer (OBS) deployments in the South Pacific.

This article is a proof of concept demonstrating the utility of MERMAID for more than mantle-scale P-wave tomography alone. Here, we showcase signals beyond mantle P waves, including S waves, surface waves, T waves, and inner- and outer-core phases. Such signals are eminently useful for myriad seismological and geophysical studies at multiple scales. As a case study, we show that we are able to obtain high-quality travel-time residuals from core phases sampling novel ray paths in the outer core.

Recovering such signals as part of our routine operations presented a welcome surprise. First, their retrieval was not a stated design goal of MERMAID, and second, it was unclear from the outset that the seismoacoustic conversion of many of those phases at the seafloor would be strong enough to generate pressure signals detectable by MERMAID's hydrophone at 1500 m depth. Nevertheless, the "extended utility" of data acquisition by autonomous diving floats is not an anomaly. Although we focus here on secondary phases that are already part of our dataset of ~240 s long triggered and automatically reported segments, many similar signals remain retrievable from MERMAID's 1 yr buffer (S. Pipatprathanporn and F. J. Simons, unpublished manuscript, 2021, see Data and Resources) and can be recovered upon request using Iridium's two-way Router-Based Unrestricted Digital Internetworking Connectivity Solutions (RUDICS) communication protocol—time, money, bandwidth, and battery-life permitting.

Historical Context and Novelty

The observation and identification of the seismic phases that we highlight here are routine on (is)land-based stations—even core-transmitted phase detection spans back more than 100 yr (Gutenberg, 1913). Likewise, ocean-bottom instruments have been used to sense Earth's free oscillations (Bécel *et al.*, 2011; Deen *et al.*, 2017), to investigate $M_L < 0$ "nanoearthquakes" (Butler, 2003), to observe slow-slip seismic events (e.g., Wallace *et al.*, 2016), and to map discontinuities both shallow (Janiszewski and Abers, 2015) and deep (Agius *et al.*, 2021) within the Earth. Global seafloor observatories have been proposed to monitor these phenomena over large spatial and long time scales (Kohler *et al.*, 2020). Water-column observations of seismoacoustic and hydroacoustic phases by hydrophones, similarly, have a respectable past (Slack *et al.*, 1999; Caplan-Auerbach *et al.*, 2001; Bohnenstiehl *et al.*, 2002; Dziak *et al.*, 2004; Smith *et al.*, 2004; Tepp and Dziak, 2021), but unlike with MERMAID, the hydrophones used in those studies were tethered at fixed locations.

The novel observations that we report here were made by MERMAID hydrophones perennially adrift in the water column of the inhospitable ocean. They thus permit entirely new, ever-changing geometries of observation, they may contain earthquakes and other events that remain undetected otherwise and that can be transmitted and received within hours of detection, and they do not require expensive ship-based instrument retrieval (but see Berger *et al.*, 2016).

Although we refer to all MERMAID records as "seismograms," they are time series of acoustic pressure, not direct measures of ground motion. The details of the instrumental response (low for a hydrophone; Joubert *et al.*, 2015) are beyond the scope of this study, as is the exact nature of the solid–fluid coupling mechanism. Some signals may be the result of multiple complex seismoacoustic conversions along the seafloor, confounded by reflections from the surface of the ocean, ocean-floor scattering, and other sources of oceanic ambient noise (e.g., Webb, 1998; Tanimoto, 2005; Gualtieri *et al.*, 2018; Nakata *et al.*, 2019). Modeling the waveforms computationally (Stephen, 1988; Komatitsch *et al.*, 2000; Cristini and Komatitsch, 2012) at the observed frequencies (high for global modeling) will require honoring near-receiver small-scale ocean-floor structure, detailed knowledge of bathymetry, large modeling domains, high-resolution meshes, and, ultimately, significant computational resources (Jamet *et al.*, 2013; Li *et al.*, 2019; Fernando *et al.*, 2020).

S Waves

Compressional waves in the solid Earth are termed *P* because they constitute the "primary" arrival. Shear motion in the Earth propagates more slowly; hence, torsional waves are referred to as *S*, for "secondary." (As to any "tertiary" or *T* arrivals, see the *T* Waves section.)

Figure 2 contains the first published examples of *S* waves recorded by MERMAID. Because shear waves do not travel as such through the ocean layer, what is actually being recorded here are the signals of their seismoacoustic (*s*-to-*P* and *S*-to-*P*) conversion at the seafloor. The strength of the conversion requires quantification (e.g., Reid *et al.*, 1973). The examples correspond to a very nearby earthquake in the epicentral distance range of 8°–14°.

Figure 2 is a record section for an M_w 6.7 Fiji Islands region earthquake at a 564.1 km depth. The seismograms are filtered between 0.1 and 0.2 Hz using a four-pole one-pass Butterworth filter, and each is normalized for consistent display. The final two digits of the recording MERMAID's serial number are noted to the left of each trace. Within this frequency band, we clearly see the arrival of both *P* and *S* waves, the theoretical travel times of which in the 1D ak135 velocity model of Kennett *et al.* (1995) are marked by black and red curves, respectively. These travel-time curves are not adjusted for bathymetry or MERMAID cruising depth because that correction uniquely applies to specific arrivals and not to entire travel-time curves. For reference, a good rule of thumb posits that, after correction for bathymetry and cruising depth, on average, phase arrivals at MERMAID are delayed by 1 s with respect to ak135. This theoretical time delay is acquired during the final few kilometers of the ray path, from seafloor to MERMAID hydrophone, which traverses the relatively slow (with an acoustic velocity of ~1.5 km/s, compared with 5.8 km/s in the topmost crustal layer of ak135) water column.

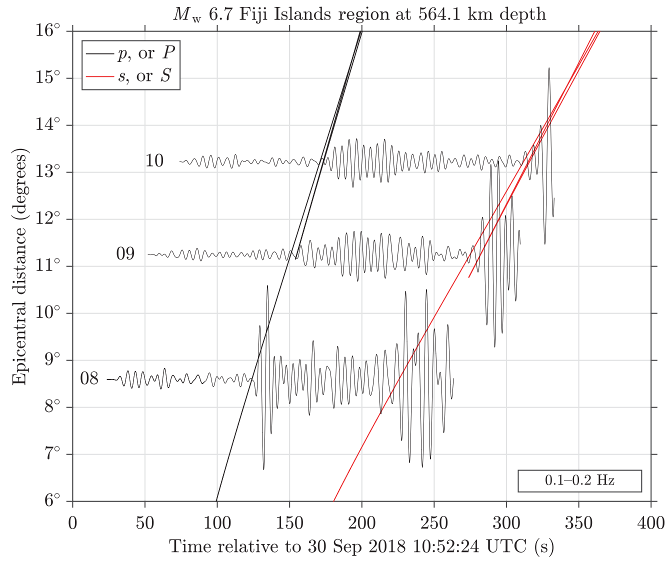

Figure 2. Low-frequency filtered MERMAID seismograms showing *S*-wave arrivals. Theoretical travel times of *P* and *S* waves in the ak135 model are marked by black and red curves, respectively.

We reiterate the point that observations of many of the phases presented in this study that arrive after the *P* wave are not extraordinary because their generation might require some exotic underlying physical process or unique setting, but rather simply because they arrived in our routine reporting time window with a length of ~240 s. In other words, for the phases shown, MERMAID simply was close enough in epicentral distance for multiple phases to arrive sufficiently shortly after the *P* wave. This fact is highlighted in the regional map of Figure 1b, in which we render three of the ray paths emanating from one earthquake in black and 10 in gray. The former correspond to the seismograms shown in Figure 2; the latter denote ray paths to MERMAIDs too distant for the *S* wave to appear in the ~240 s segment that is transmitted automatically. Studying *S*-wave detection thresholds will require systematically reporting longer data segments or requesting them from MERMAID's 1 yr buffer.

Surface Waves

Figure 3 is the first published example of a surface wave recorded by MERMAID. It shows a clear surface-wave detection in a detrended but otherwise unfiltered MERMAID seismogram. Its dominant period appears to be around 10 s, at the

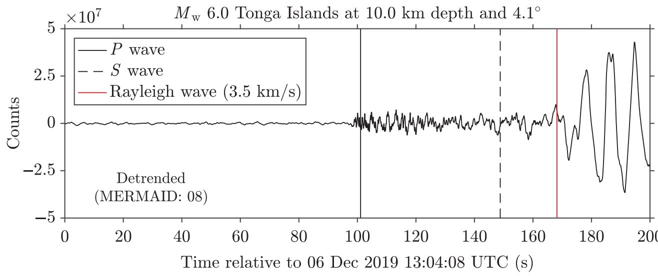

Figure 3. Detrended but otherwise unfiltered MERMAID seismogram showing the arrival of a high-amplitude surface wavetrain. Black vertical lines mark the theoretical arrival times of the *P* (solid) and *S* (dashed) waves in ak135. The red line marks the theoretical arrival time of a surface wave traveling with a phase velocity of 3.5 km/s.

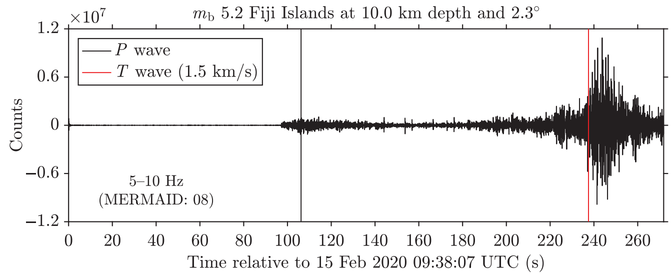

Figure 4. MERMAID seismogram filtered between 5 and 10 Hz, showing a high-amplitude *T* wave. Theoretical arrival times for the *P* wave in ak135 and for a phase with a horizontal velocity of the average sound speed in water, 1.5 km/s, are marked by black and red vertical lines, respectively.

likely edge of MERMAID's linear amplitude response. We label it generically as a Rayleigh wave, with displacement components normal to the seafloor that are capable of generating seismoacoustic pressure conversions. The corresponding event was a large (M_w 6.0), shallow (10 km), and proximal (4.1°) earthquake in the Tonga Islands. Plotted as vertical lines from left to right are the theoretical arrival times as computed in ak135 of the *P* and *S* waves, as black solid and dashed lines, respectively. The solid red line predicts the arrival of a surface wave with a horizontal speed of 3.5 km/s, which would correspond to a 25 s fundamental-mode Rayleigh wave in ak135 (Kennett, 2001). No large arrival associated with the *S* wave is detected in this unfiltered seismogram.

Surface-wave amplitudes decay cylindrically with distance, more slowly than the spherically-spreading body waves. The large amplitude of the surface wave presented here means that we expect other examples in the MERMAID data buffer. In this case, a MERMAID was drifting near enough to the source to record it. It arrived within ~100 s of the *P* wave and thus was automatically included in the ~240 s seismogram reported by default. The two-way Iridium communication system built into every float allows us to request from MERMAID's 1 yr data buffer any segments of interest that might contain surface waves.

Waves with *P-SV* polarization traveling along a fluid–solid interface can also be Scholte waves (Kugler *et al.*, 2007). These relatively high-frequency (for surface waves) and low-velocity waves may prove especially useful for shallow seismic studies, for example, to probe the depth extent and seismic wavespeeds of seafloor sediments (Nolet and Dorman, 1996). Hable *et al.* (2019) detected both Rayleigh and Scholte waves using OBSs in the Indian Ocean. Within the 0.1–0.3 Hz frequency band (in which MERMAID also has good sensitivity), both displayed linear moveouts with velocities of 3–4 and 0.8–1.5 km/s, respectively. These same authors also found that within this frequency band Scholte-wave amplitudes dominate Rayleigh-wave amplitudes and propagate over distances exceeding 1000 km. Our findings motivate a future hunt for Scholte waves later in our MERMAID seismograms.

T Waves

Land-based seismometers often pick up arrivals of a tertiary or *T* phase. The name likely first appeared in print when Linehan (1940) called them a "third unidentified group" arriving after the *P* and *S* waves from teleseismic earthquakes. These are acoustic waves that propagate within the Sound Fixing And Ranging (SOFAR) channel (Munk *et al.*, 1995), a minimum-velocity waveguide that traps sound from a variety of sources, including earthquakes, and permits its efficient propagation across entire ocean basins (Okal, 2008).

Typically, *T* waves are emergent rather than impulsive. When generated by earthquakes, their shape depends on a variety of factors including multipathing in the solid Earth before reaching the seafloor, and seafloor geometries that result in the inefficient transfer of (sub)vertically traveling seismic energy into horizontally propagating *T*-wave energy without multiple surface-seafloor reverberations near the conversion site (e.g., Talandier and Okal, 1998, 2001). These and other complex scattering effects (Fox *et al.*, 1993; Park *et al.*, 2001) tend to defocus the wavetrain and produce a characteristic spindle-like shape (Jamet *et al.*, 2013). In MERMAID seismograms, *T* waves are most easily distinguishable from the coda that follows *P* arrivals by their high amplitudes, high-frequency content, and tapered envelope.

Figure 4 shows a high-frequency 5–10 Hz filtered MERMAID seismogram with an example of a *T* wave with its maximum amplitude around 240 s. The corresponding event was a local (2.3°) and shallow (10 km) m_b 5.2 Fiji Islands earthquake. The theoretical arrival time of the *P* wave is marked with a black vertical line. We attribute the ~10 s observed advance to earthquake mislocation. In red, we mark the arrival time of a phase traveling horizontally at 1.5 km/s. Various features make us confident that this is in fact a *T* wave: it is of very high frequency; its amplitude is large compared with that of the *P*-wave arrival, perhaps due in part to the proximity of this event

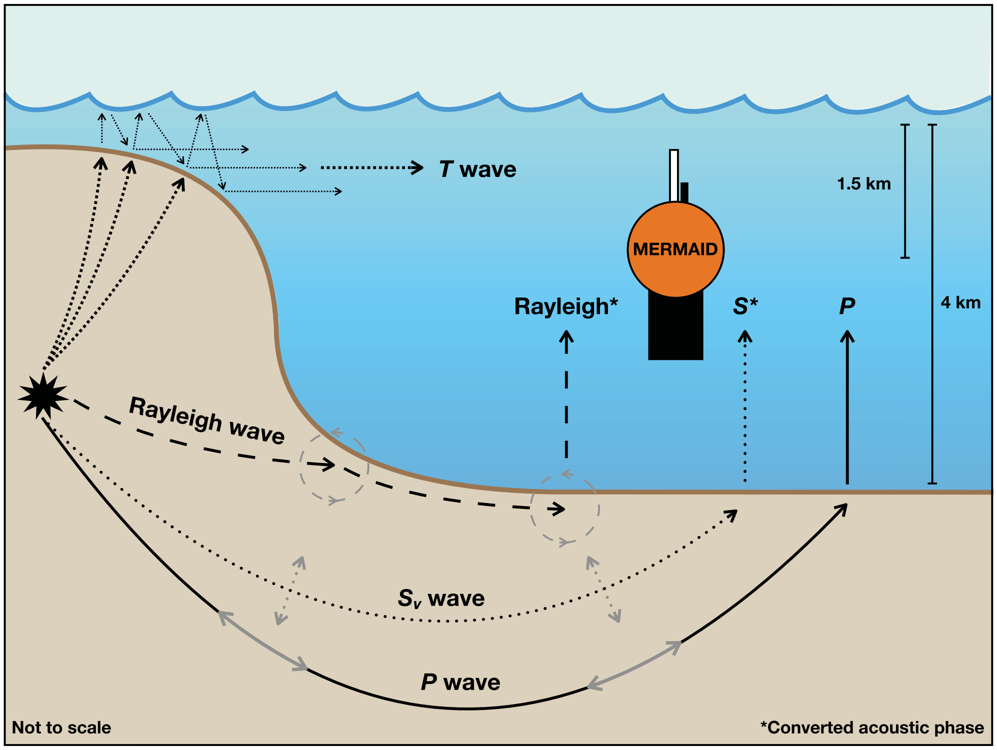

Figure 5. Example ray paths from an earthquake, in black with particle motion in gray, through conversion to acoustic phases at the seafloor, to propagation and recording within the water column by MERMAID, for the phases shown in Figures 2–4.

(see also Slack *et al.*, 1999); and most notably, its arrival is emergent and its decay similarly tapered. In contrast, body waves, especially at these short distances, arrive impulsively.

The SOFAR channel generally has its axis around 1000 m depth (Munk *et al.*, 1995), and MERMAID's usual parking depth of 1500 m, largely a choice of convenience, though easily changed, was meant to mostly avoid the detection of *T* waves, which would trigger unnecessary surfacing; they are loud and abundant in the global oceans. Furthermore, MERMAID's current onboard detection algorithm (Sukhovich *et al.*, 2011, 2014) rather explicitly rejects *T* waves. Indeed, for the example shown in Figure 4, the *P* wave around 100 s, not the *T* wave around 240 s, provided the trigger for MERMAID's ascent and signal transmission.

Nevertheless, recording *T* waves in the oceans has far-reaching utility for seismic studies and beyond, including tracking icebergs (Chapp *et al.*, 2005), monitoring submarine volcanic eruptions (Metz *et al.*, 2018), and Comprehensive Nuclear-Test-Ban Treaty verification (Talandier and Okal, 2001). Most recently, Wu *et al.* (2020) demonstrated that decadal-scale ocean-warming trends are manifest in the differences in travel-time delays between *T* waves generated by repeating earthquakes. Because MERMAID's parking depth may be shoaled using simple commands relayed via satellite, adjustments can be made to the detection algorithm, and a forthcoming redesign (dubbed the "Lander") would have it act as a temporary ocean-bottom hydrophone, MERMAID arrays may well become pivotal as *T*-phase "stations" to monitor our changing climate.

From Local to Global Phases

A schematic summarizing the paths that *P*, *S*, Rayleigh, and *T* waves may take from an earthquake source to a MERMAID adrift is given in Figure 5. The float (not to scale) is centered at 1500 m depth, its common cruising depth, in a 4 km deep average ocean. Rayleigh and *S* waves are labeled with an asterisk to remind the reader that MERMAID records their acoustic conversions, which travel more or less vertically through the water column from the seafloor to the hydrophone. The *T* wave shown here is generated via "downslope conversion"—multiply reflected between the surface and a sloping seafloor (Johnson *et al.*, 1963)—and it is the only phase that travels horizontally and over any substantial distance due to its entrapment within the SOFAR channel. A sense of scale is lost in this picture in which we attempted to draw phases taking widely different paths on their journey to MERMAID. The paths of core phases as discussed next are drawn to scale in Figure 6. Figure 5 reminds us that the final leg of any phase travels as a pressure wave from the seafloor to MERMAID's hydrophone.

Core Phases

Inner-core phases

Figure 7 displays a *PKIKP* phase arrival corresponding to an M_w 6.1 Hindu Kush region, Afghanistan, earthquake. The seismogram is filtered between 1 and 2 Hz. We show a 30 s window of the seismogram centered on the theoretical arrival of *PKIKP* in an ak135 model adjusted for 2014 General Bathymetric Chart of the Oceans (GEBCO; Weatherall *et al.*, 2015) bathymetry and MERMAID's depth at the time of recording. Our adjusted *PKIKP* residual, t^*_{res}, is marked by a solid black vertical line bracketed on either side by dashed black vertical lines representing twice the standard deviation of our timing-error estimate, $2\mathrm{St.dev.}_{\mathrm{err}}$. Event parameters are inset in the upper boxes, and signal criteria are in the lower.

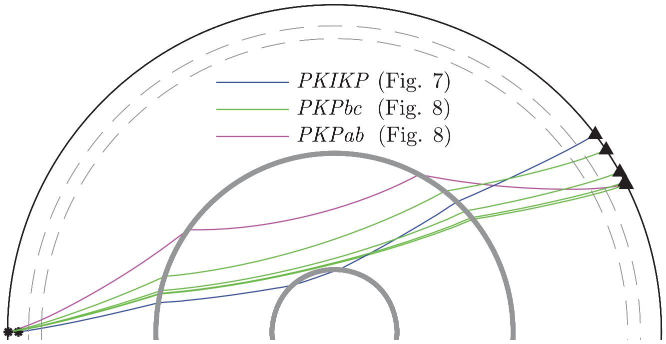

Figure 6. Ray paths in Earth model ak135 corresponding to the phase arrivals shown in Figures 7 and 8; they are plotted in the same colors. *PKIKP* can be seen in Figure 7. The primary arrivals in Figure 8 represent *PKPbc* phases that sense the deepest regions of the outer core. Here, we plot the ray paths corresponding to the green phase branch for all four seismograms in Figure 8. We draw a single *PKPab* ray path for the top trace in Figure 8, in which we identify this shallow outer-core phase.

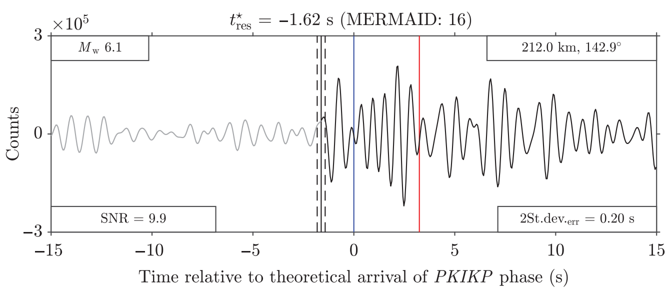

Figure 7. MERMAID seismogram filtered between 1 and 2 Hz, showing an inner-core *PKIKP* phase arrival. The timing is relative to the theoretical arrival of *PKIKP* (blue vertical line) in an ak135 model adjusted for bathymetry and MERMAID's parking depth. The black vertical line marks the travel-time residual with dashed lines for uncertainty. The red line indicates the theoretical arrival time of *PKiKP*.

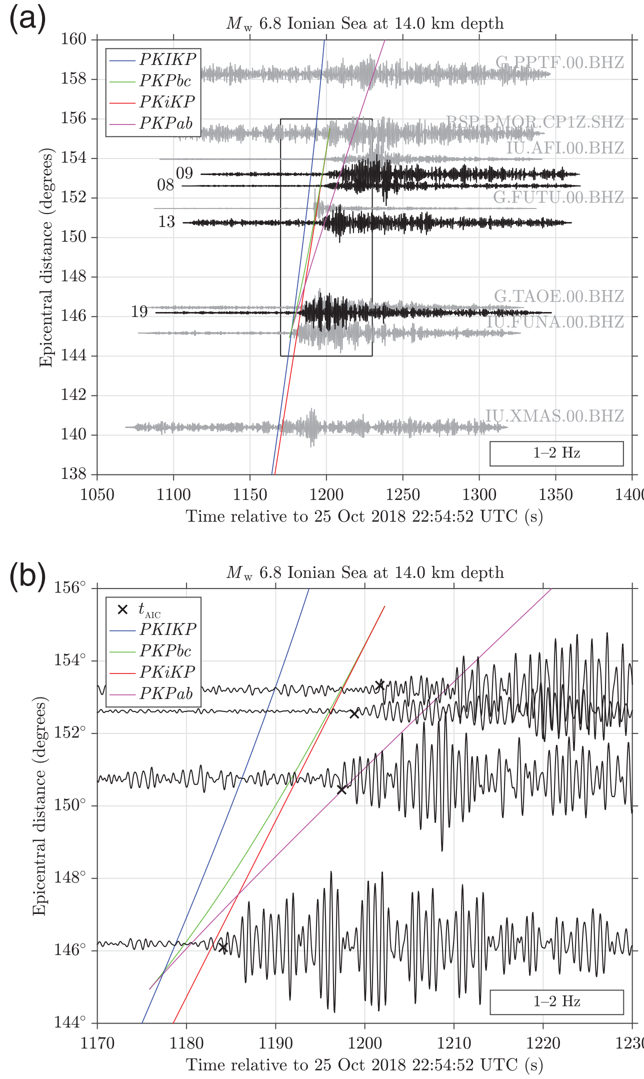

Figure 8. Seismograms filtered between 1 and 2 Hz showing outer-core phase arrivals. Colored curves plot the theoretical travel times of core phases in ak135: *PKIKP* (blue); *PKPbc* (green); *PKiKP* (red); and *PKPab* (magenta). (a) MERMAID traces (black) and traces from nearby island stations (gray). (b) Zoom-in around the expected arrivals of core phases in MERMAID seismograms only. Crosses mark the observed travel times, t_{AIC}, determined following the method of Simon *et al.* (2020). All MERMAID traces display an arrival that we associate with *PKPbc*, and the top trace (MERMAID 09) exhibits a secondary phase marking the arrival of *PKPab*.

We define the signal-to-noise ratio (SNR) as the ratio of variances of the signal (black) and noise (gray) segments, and we estimate 2St.dev.$_{err}$ using Method 1 of Simon *et al.* (2020). The red vertical line at 3.25 s marks the theoretical offset of the travel time of the secondary inner-core *PKiKP*-reflected phase, which we do not detect in this seismogram.

Figure 7 was recorded with a source-receiver geometry (212.0 km depth at 142.9°) for which only inner-core *PKIKP* and *PKiKP* phases are predicted to arrive in the time window of the seismogram. Next, we discuss 10 more MERMAID seismograms that triggered on core phases, but which were recorded at epicentral distances beyond the *PKP* caustic (~145°), in which outer-core *PKPbc* and *PKPab* phases are also predicted to arrive close in time to their inner-core complements. In all cases, we are able to recover high-quality travel-time residuals from phases that sample the core at multiple depths, along novel ray paths.

Outer-core phases

Figure 8 presents record sections corresponding to an M_w 6.8 earthquake under the Ionian Sea. Figure 8a plots MERMAID seismograms in black alongside seismograms from nearby island stations in gray, whereas Figure 8b focuses only on

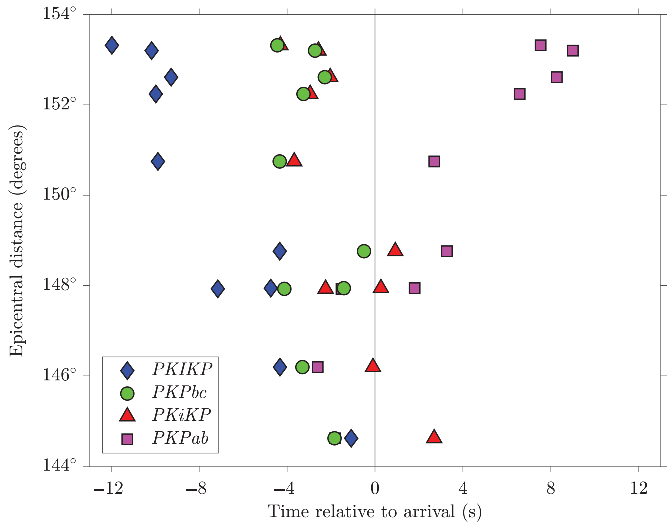

Figure 9. Core-phase-adjusted "model residuals" (ak135 prediction minus observation) for MERMAID seismograms predicted to contain both inner- and outer-core phase arrivals. The plot helps identify the phases associated with our arrival-time picks in Figure 8, using the same color scheme as the travel-time curves and further differentiated by marker. Only the outer-core *PKPbc* and inner-core *PKiKP* model residuals exhibit no trend with distance, and either of them could trigger our picker. Because *PKiKP* is a low-amplitude reflection, MERMAID must be recording *PKPbc*-phase arrivals.

the MERMAID seismograms in the truncated distance range noted by the box in Figure 8a. Station names of nearby island seismometers are annotated after their corresponding traces in Figure 8a, whereas the unique portion of the serial number of the recording MERMAID is marked before its associated black trace in Figure 8a and outside the right-ordinate axis in Figure 8b. Gray traces in Figure 8a were trimmed to approximate the default-length MERMAID seismograms, and all traces in both figures were tapered using a 0.1-ratio cosine-taper (Tukey) window. This figure shows that MERMAID records data with similar fidelity to island seismic stations in the same oceanic neighborhood.

Four potential phases arrive in the time window of Figure 8b. Crosses mark our travel-time picks, t_{AIC}, obtained following the method of Simon *et al.* (2020). We again color-code the four core-phase travel-time curves, that is, blue for *PKIKP*, green for *PKPbc*, red for *PKiKP*, and magenta for *PKPab*. We hypothesize that when multiple core-phase arrivals coexist in the seismogram, the dominant phase actually being detected is *PKPbc*. This is based on a few key observations. First, we can reject the possibility that the inner-core reflection *PKiKP* was detected because *PKPbc* is a higher-amplitude phase at the relevant distances (e.g., fig. 8 of Ohtaki and Kaneshima, 2015). Second, arrivals associated with either of the *PKP* branches are predicted to have higher SNRs than *PKIKP*. The former remain in the extremely low-attenuating outer core, in which the bulk quality factor Q_κ is often approximated to be infinity. The latter dive into the comparatively highly attenuating (Romanowicz and Mitchell, 2015) inner core and are therefore expected to have lower amplitudes. Finally, *PKPbc* arrives before *PKPab*, and therefore the latter could be drowned out by the persistent reverberations in the water column that often dominate MERMAID seismograms for tens of seconds after the first arrival.

To test the hypothesis that we are indeed observing *PKPbc* arrivals in Figure 8b, Figure 9 plots, for various core phases, the difference between the theoretical arrival times and the observations (individually adjusted for bathymetry and MERMAID cruising depth). We call this measure an adjusted "model residual" because it has the opposite sign of the travel-time residual quoted in Figure 7, which refers to observation minus prediction. The time picks were computed in the same manner as in Figure 7, except within a window centered on *PKPbc* rather than *PKIKP*. The theoretical travel-time phase branches are colored as in Figure 8 and further differentiated by their markers. We see that the model residuals of both *PKPbc* and *PKiKP* phases are largely independent of epicentral distance and fall within the interval ± 4.3 s. In contrast, the inner-core *PKIKP* and outer-core *PKPab* phases display generally negative and positive model residuals, respectively, which increase with distance. Hence, Figure 9 proves our hypothesis.

To test for the existence of phase-picking bias introduced by our windowing, we repeated the calculation depicted in Figure 9 using *PKIKP*-centered windows and found no significant difference compared with *PKPbc*-centered windows. Barring two rather emergent signals with arrival-time picks that proved sensitive to the choice of the center of the window, any differences were within 0.1 s. As long as the window included the later-arriving outer-core *PKPbc* phase, the Simon *et al.* (2020) phase picker selected it over *PKIKP*. However, we were able to detect later *PKPab* arrivals in some MERMAID seismograms by running our picker recursively on time-shifted windows. See, for example, the top trace in Figure 8 in which both outer-core *PKPbc* and *PKPab* phases could be discerned.

After 1D travel-time adjustments are made and bathymetry and cruising depth are accounted for we find that the *PKPbc* phases in our catalog display a positive bias. All are delayed with respect to their theoretical travel times. Their mean residual is +2.7 s for travel times that range between 1150.4 and 1197.3 s, representing an average travel-time perturbation of 0.2%.

In this section, we have shown that MERMAID is able to autonomously report data from core phases sampling novel ray paths in the core, which we can identify and for which we can obtain travel-time residuals with high confidence. We do note that we have yet to identify *PcP* or *Pdif* phases in the MERMAID catalog.

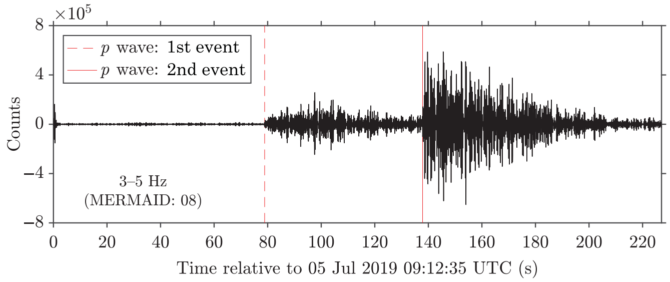

Figure 10. MERMAID seismogram showing what we interpret to be two *p*- (or possibly *P*-) wave arrivals from two separate and unidentified events. The corresponding event information is missing from the global National Earthquake Information Center (NEIC) Preliminary Determination of Epicenters (PDE) Bulletin. Dashed and solid red vertical lines mark our time picks for both phases.

Unidentified (Local) Events

We end this tour of the data that MERMAID has been returning in addition to teleseismic *P* waves with an example of a pair of unidentified events. Figure 10 shows two distinct arrivals: the first near 80 s and the second, larger one, arriving about 60 s later. Neither of these match with any theoretical phase-arrival times associated with any known events in the National Earthquake Information Center (NEIC) Preliminary Determination of Epicenters (PDE) Bulletin. Our interpretation is that these two signals are both *p*- (or, less likely, *P*-) wave arrivals from two distinct very nearby events. We mark their picked arrival times as dashed and solid red vertical lines, picked within 30 s windows (centered first on 80 s and then on 140 s) of the seismogram filtered between 3 and 5 Hz in Figure 10.

Both signals, especially the second one, are impulsive, implying that the latter is not a *T* wave associated with the earlier signal. Discrimination based on this simple observation is not foolproof. Some rather impulsive *T* waves have been recorded in French Polynesia by the Réseau Sismique Polynésien. These were generated by various sources, including earthquakes (Talandier and Okal, 1998) and explosive volcanism (Talandier and Okal, 2001).

It is also unlikely that the second, larger arrival is an *S* wave because it is of very high frequency, not expected for a shear conversion, and the *S*–*P* delay time would imply an epicentral distance of approximately 500 km. Similar reasoning argues against it comprising surface waves. No other MERMAID in the array reported these events, further supporting our assertion of their extremely local nature. Both arrivals remain very distinct at frequencies up to 10 Hz (not shown here), which is uncommon for identified MERMAID signals, except in the case of local events (as in Fig. 4).

Hence, our conclusion is that Figure 10 depicts two distinct arrivals, from two very proximal earthquakes. Hundreds of similar examples currently exist in the catalog of automatically-reported segments, implying that MERMAID may be used for studies of regional and local seismicity.

Conclusion

MERMAID is able to record more than just teleseismic *P* waves, with the fidelity required to conduct high-quality seismic studies at multiple scales. We showed the first published examples of *S* and Rayleigh waves recorded by MERMAID. We used the travel-time residual and timing-uncertainty estimation schemes of Simon *et al.* (2020) to prove that both inner- and outer-core travel-time residuals are recoverable from the MERMAID catalog. The authors similarly analyzed the complementary set of mantle *P* waves in a separate study (J. D. Simon *et al.*, unpublished manuscript, 2021, see Data and Resources). We ended with an example of unidentified events—*P* waves for which no corresponding events were found in the NEIC PDE Bulletin. Beyond their utility for seismology and geophysics, the signals shown here will guide the study of seismic–acoustic coupling at the seafloor to ensure that computer modeling faithfully reproduces those interactions at frequencies around ~1 Hz.

Every signal shown in this study was sent by MERMAID without human intervention because it triggered the onboard detection algorithm. None of the signals discussed here were requested from the buffer. For us to see these phases, a *P* or *PKP* wave had to have triggered the detection algorithm, and the later-arriving phases had to arrive within ~140 s after that trigger. At present, the automated algorithm is tuned to identify and report ~1 Hz *P* waves, and it defaults to align the triggering seismic signal at around 100 s into the ~240 s transmitted seismogram. Seismic records in this article that display multiple phase arrivals all include a *P*- or *PKP*-wave arrival preceding the secondary and tertiary phases further discussed. Excluding the zoomed-in core phases, these seismograms were not truncated for display purposes.

There are likely many more similar phases that were recorded but not (yet) reported by MERMAID. Requesting data segments of interest from floats currently operational remains an option for a period of 1 yr. Beyond such requests from MERMAIDs already deployed, adjustments to the detection algorithm may be made to yield other and different data, which are useful for seismic studies from the local to the global scale. MERMAID buffers will be open for time-series requests from the broader scientific community. Useful to some, they will ultimately be available to all. At this moment, scientific requests are welcome by email to the first author.

Data and Resources

The Mobile Earthquake Recorder in Marine Areas by Independent Divers (MERMAID) International Federation of Digital Seismograph Networks (FDSN) network code is MH (https://fdsn.org/networks/detail/MH/). The data discussed here are in the processing pipeline for public distribution by the Incorporated

Research Institutions for Seismology Data Management Center (IRIS DMC; http://ds.iris.edu/ds/nodes/dmc/). Beyond software written by the authors, we relied on irisFetch. Events version 2.0.10, available from IRIS, to query the National Earthquake Information Center (NEIC) Preliminary Determination of Epicenters (PDE) Bulletin (https://www.sciencebase.gov/catalog/item/588b90dae4b0ad6732402989) for recent events, and MatTaup written by Qin Li in 2002 to compute theoretical travel times and to plot their ray paths in the ak135 model of Kennett *et al.* (1995). We maintain versions of these codes and all other software developed and used in this study at https://github.com/joelsimon/omnia/. Seismic data from "nearby" island stations in the South Pacific (Fig. 8a) were provided by the Institut de Physique du Globe de Paris (IPGP; http://centrededonnees.ipgp.fr), the IRIS DMC, and Olivier Hyvernaud at the French Commissariat à l'Energie Atomique et aux Energies Alternatives. A near real-time map of the entire South Pacific Plume Imaging and Modeling (SPPIM) project array is available at http://www.earthscopeoceans.org. Data about MERMAID deployments in the South Pacific are available at DOI: 10.17600/18000519 and DOI: 10.17600/18000882. All websites referenced in this section were last accessed in May 2021. The unpublished manuscript by S. Pipatprathanporn, and F. J. Simons, 2021, "One year of sound recorded by a MERMAID float in the Pacific: Hydroacoustic earthquake signals and infrasonic ambient noise", was submitted to *Geophys. J. Int.* and J. D. Simon, F. J. Simons, and J. C. E. Irving, 2021, "Recording earthquakes for tomographic imaging of the mantle beneath the South Pacific by autonomous MERMAID floats", was submitted to *Geophys. J. Int.*

Declaration of Competing Interests

The authors acknowledge that there are no conflicts of interest recorded.

Acknowledgments

Part of this work was supported by the National Science Foundation (DGE-1656466 to J. D. S., and OCE-1917058 and EAR-1644399 to F. J. S. and J. C. E. I.). The authors commend Ifremer, Genavir, and Commander Jean-François Barazer and his crew aboard the research Vessel (R/V) *Alis* for a seamless series of Mobile Earthquake Recorder in Marine Areas by Independent Divers (MERMAID) deployments in the South Pacific (see Data and Resources). The authors thank Editor-in-Chief Allison Bent and two anonymous reviewers whose comments greatly improved this article.

References

Agius, M. R., C. A. Rychert, N. Harmon, S. Tharimena, and J.-M. Kendall (2021). A thin mantle transition zone beneath the equatorial Mid-Atlantic Ridge, *Nature* **589,** no. 7843, 562–566, doi: 10.1038/s41586-020-03139-x.

Bécel, A., M. Laigle, J. Diaz, J.-P. Montagner, and A. Hirn (2011). Earth's free oscillations recorded by free-fall OBS ocean-bottom seismometers at the Lesser Antilles subduction zone, *Geophys. Res. Lett.* **38,** no. 24, L24305, doi: 10.1029/2011GL049533.

Berger, J., G. Laske, J. Babcock, and J. Orcutt (2016). An ocean-bottom seismic observatory with near real-time telemetry, *Earth Space Sci.* **3,** 68–77, doi: 10.1002/2015EA000137.

Bohnenstiehl, D. R., M. Tolstoy, R. P. Dziak, C. G. Fox, and D. K. Smith (2002). Aftershock sequences in the mid-ocean ridge environment: An analysis using hydroacoustic data, *Tectonophysics* **354,** 49–70, doi: 10.1016/S0040-1951(02)00289-5.

Butler, R. (2003). The Hawaii-2 Observatory: Observation of nanoearthquakes, *Seismol. Res. Lett.* **74,** no. 3, 290–297, doi: 10.1785/gssrl.74.3.290.

Caplan-Auerbach, J., C. Fox, and F. K. Duennebier (2001). Hydroacoustic detection of submarine landslides on Kilauea volcano, *Geophys. Res. Lett.* **28,** no. 9, 1811–1813, doi: 10.1029/2000GL012545.

Chapp, E., D. R. Bohnenstiehl, and M. Tolstoy (2005). Sound-channel observations of ice-generated tremor in the Indian Ocean, *Geochem. Geophys. Geosys.* **6,** no. 6, Q06003 , doi: 10.1029/2004GC000889.

Cristini, P., and D. Komatitsch (2012). Some illustrative examples of the use of a spectral-element method in ocean acoustics, *J. Acoust. Soc. Am.* **131,** no. 3, EL229–EL235, doi: 10.1121/1.3682459.

Deen, M., E. Wielandt, E. Stutzmann, W. Crawford, G. Barruol, and K. Sigloch (2017). First observation of the Earth's permanent free oscillations on ocean bottom seismometers, *Geophys. Res. Lett.* **44,** no. 21, 10,988–10,996, doi: 10.1002/2017GL074892.

Dziak, R. P., D. R. Bohnenstiehl, H. Matsumoto, C. G. Fox, D. K. Smith, M. Tolstoy, T.-K. Lau, J. H. Haxel, and M. J. Fowler (2004). *P*- and *T*-wave detection thresholds, *Pn* velocity estimate, and detection of lower mantle and core *P*-waves on ocean sound-channel hydrophones at the Mid-Atlantic Ridge, *Bull. Seismol. Soc. Am.* **94,** no. 2, 665–677, doi: 10.1785/0120030156.

Fernando, B., K. Leng, and T. Nissen-Meyer (2020). Oceanic high-frequency global seismic wave propagation with realistic bathymetry, *Geophys. J. Int.* **222,** no. 2, 1178–1194, doi: 10.1093/gji/ggaa248.

Fox, C. G., R. P. Dziak, H. Matsumoto, and A. E. Schreiner (1993). Potential for monitoring low-level seismicity on the Juan de Fuca ridge using military hydrophone arrays, *Mar. Tech. Soc. J.* **27,** no. 4, 22–30.

General Bathymetric Chart of the Oceans (GEBCO) Bathymetric Compilation Group (2019). The GEBCO_2019 grid—A continuous terrain model of the global oceans and land, *Technical Report*, British Oceanographic Data Centre, National Oceanography Centre, NERC, United Kingdom.

Gualtieri, L., S. J. Camargo, S. Pascale, F. M. E. Pons, and G. Ekström (2018). The persistent signature of tropical cyclones in ambient seismic noise, *Earth Planet. Sci. Lett.* **484,** 287–294, doi: 10.1016/j.epsl.2017.12.026.

Gutenberg, B. (1913). Über die Konstitution des Erdinnern, erschlossen aus Erdbebenbeobachtungen, *Physikalische Zeitschrift* **14,** 1217–1218 (in German).

Hable, S., K. Sigloch, E. Stutzmann, S. Kiselev, and G. Barruol (2019). Tomography of crust and lithosphere in the western Indian Ocean from noise cross-correlations of land and ocean bottom seismometers, *Geophys. J. Int.* **219,** no. 2, 924–944, doi: 10.1093/gji/ggz333.

Hello, Y., and G. Nolet (2020). Floating seismographs (MERMAIDS), in *Encyclopedia of Solid Earth Geophysics*, H. K. Gupta (Editor), Encyclopedia of Earth Sciences, 1–6, doi: 10.1007/978-3-030-10475-7_248-1.

Hello, Y., A. Ogé, A. Sukhovich, and G. Nolet (2011). Modern MERMAIDs: New floats image the deep Earth, *Eos Trans. AGU* **92,** no. 40, 337–338, doi: 10.1029/2011EO400001.

Jamet, G., C. Guennou, L. Guillon, C. Mazoyer, and J.-Y. Royer (2013). *T*-wave generation and propagation: A comparison between data and spectral element modeling, *J. Acoust. Soc. Am.* **134,** no. 4, 3376–3385, doi: 10.1121/1.4818902.

Janiszewski, H. A., and G. A. Abers (2015). Imaging the plate interface in the Cascadia seismogenic zone: New constraints from offshore receiver functions, *Seismol. Res. Lett.* **86,** no. 5, 1261–1269, doi: 10.1785/0220150104.

Johnson, R. H., J. Northrop, and R. Eppley (1963). Sources of Pacific *T* phases, *J. Geophys. Res.* **68,** no. 14, 4251–4260, doi: 10.1029/JZ068i014p04251.

Joubert, C., G. Nolet, S. Bonnieux, A. Deschamps, J.-X. Dessa, and Y. Hello (2016). *P*-delays from floating seismometers (MERMAID), part I: Data processing, *Seismol. Res. Lett.* **87,** no. 1, 73–80, doi: 10.1785/0220150111.

Joubert, C., G. Nolet, A. Sukhovich, A. Ogé, J.-F. Argentino, and Y. Hello (2015). Hydrophone calibration at very low frequencies, *Bull. Seismol. Soc. Am.* **105,** no. 3, 1797–1802, doi: 10.1785/0120140265.

Kennett, B. L. N. (2001). *The Seismic Wavefield, Vol. I: Introduction and Theoretical Development*, Cambridge University Press, Cambridge, United Kingdom.

Kennett, B. L. N., E. R. Engdahl, and R. Buland (1995). Constraints on seismic velocities in the Earth from traveltimes, *Geophys. J. Int.* **122,** no. 1, 108–124, doi: 10.1111/j.1365-246X.1995.tb03540.x.

Kohler, M. D., K. Hafner, J. Park, J. C. E. Irving, J. Caplan-Auerbach, J. Collins, J. Berger, A. M. Tréhu, B. Romanowicz, and R. L. Woodward (2020). A plan for a long-term, automated, broadband seismic monitoring network on the global seafloor, *Seismol. Res. Lett.* **91,** no. 3, 1343–1355, doi: 10.1785/0220190123.

Komatitsch, D., C. Barnes, and J. Tromp (2000). Wave propagation near a fluid–solid interface: A spectral-element approach, *Geophysics* **65,** no. 2, 623–631, doi: 10.1190/1.1444758.

Kugler, S., T. Bohlen, T. Forbriger, S. Bussat, and G. Klein (2007). Scholte-wave tomography for shallow-water marine sediments, *Geophys. J. Int.* **168,** no. 2, 551–570, doi: 10.1111/j.1365-246X.2006.03233.x.

Li, Q., G. Wu, J. Wu, and P. Duan (2019). Finite difference seismic forward modeling method for fluid–solid coupled media with irregular seabed interface, *J. Geophys. Eng.* **16,** no. 1, 198–214, doi: 10.1093/jge/gxy017.

Linehan, D. (1940). Earthquakes in the West Indian region, *Eos Trans. AGU* **21,** no. 2, 229–232, doi: 10.1029/TR021i002p00229.

Metz, D., A. B. Watts, I. Grevemeyer, and M. Rodgers (2018). Tracking submarine volcanic activity at Monowai: Constraints from long-range hydroacoustic measurements, *J. Geophys. Res.* **123,** no. 9, 7877–7895, doi: 10.1029/2018JB015888.

Munk, W., P. Worcesterm, and C. Wunsch (1995). *Ocean Acoustic Tomography*, Cambridge Monographs on Mechanics, Cambridge University Press, Cambridge, United Kingdom, doi: 10.1017/CBO9780511666926.

Nakata, N., L. Gualtieri, and A. Fichtner (2019). *Seismic Ambient Noise*, Cambridge University Press, Cambridge, United Kingdom.

Nolet, G., and L. M. Dorman (1996). Waveform analysis of Scholte modes in ocean sediment layers, *Geophys. J. Int.* **125,** no. 2, 385–396, doi: 10.1111/j.1365-246X.1996.tb00006.x.

Nolet, G., Y. Hello, S. van der Lee, S. Bonnieux, M. C. Ruiz, N. A. Pazmino, A. Deschamps, M. M. Regnier, Y. Font, Y. J. Chen, *et al.* (2019). Imaging the Galápagos mantle plume with an unconventional application of floating seismometers, *Sci. Rep.* **9,** 1326, doi: 10.1038/s41598-018-36835-w.

Ohtaki, T., and S. Kaneshima (2015). Independent estimate of velocity structure of Earth's lowermost outer core beneath the northeast Pacific from *PKiKP–PKPbc* differential traveltime and dispersion in *PKPbc*, *J. Geophys. Res.* **120,** no. 11, 7572–7586, doi: 10.1002/2015JB012140.

Okal, E. A. (2008). The generation of *T* waves by earthquakes, *Adv. Geophys.* **49,** 1–65, doi: 10.1016/S0065-2687(07)49001-X.

Park, M., R. I. Odom, and D. J. Soukup (2001). Modal scattering: A key to understanding oceanic *T*-waves, *Geophys. Res. Lett.* **28,** no. 17, 3401–3404, doi: 10.1029/2001GL013472.

Reid, I., M. Reichle, J. Brune, and H. Bradner (1973). Microearthquake studies using sonobuoys: Preliminary results from the Gulf of California, *Geophys. J. Int.* **34,** no. 3, 365–379, doi: 10.1111/j.1365-246X.1973.tb02401.x.

Romanowicz, B. A., and B. J. Mitchell (2015). Deep Earth structure: *Q* of the Earth from crust to core, in *Treatise on Geophysics*, B. Romanowicz and A. M. Dziewoński (Editors), Vol. 1, Elsevier, Amsterdam, The Netherlands, 789–827, doi: 10.1016/B978-0-444-53802-4.00021-X.

Simon, J. D., F. J. Simons, and G. Nolet (2020). Multiscale estimation of event arrival times and their uncertainties in hydroacoustic records from autonomous oceanic floats, *Bull. Seismol. Soc. Am.* **110,** no. 3, 970–997, doi: 10.1785/0120190173.

Simons, F. J., G. Nolet, J. M. Babcock, R. E. Davis, and J. A. Orcutt (2006). A future for drifting seismic networks, *Eos Trans. AGU* **87,** no. 31, 305–307, doi: 10.1029/2006EO310002.

Simons, F. J., G. Nolet, P. Georgief, J. M. Babcock, L. A. Regier, and R. E. Davis (2009). On the potential of recording earthquakes for global seismic tomography by low-cost autonomous instruments in the oceans, *J. Geophys. Res.* **114,** no. B05307, doi: 10.1029/2008JB006088.

Slack, P. D., C. G. Fox, and R. P. Dziak (1999). *P* wave detection thresholds, P_n velocity estimates, and *T* wave location uncertainty from oceanic hydrophones, *J. Geophys. Res.* **104,** no. B6, 13,061–13,072.

Smith, D. K., R. P. Dziak, H. Matsumoto, C. G. Fox, and M. Tolstoy (2004). Autonomous hydrophone array monitors seismic activity at northern Mid-Atlantic Ridge, *Eos Trans. AGU* **85,** no. 1, 1–5, doi: 10.1029/2004EO010001.

Stephen, R. A. (1988). A review of finite difference methods for seismo-acoustics problems at the seafloor, *Rev. Geophys.* **26,** no. 3, 445–458, doi: 10.1029/RG026i003p00445.

Sukhovich, A., S. Bonnieux, Y. Hello, J.-O. Irisson, F. J. Simons, and G. Nolet (2015). Seismic monitoring in the oceans by autonomous floats, *Nat. Commun.* **6,** 8027, doi: 10.1038/ncomms9027.

Sukhovich, A., J.-O. Irisson, J. Perrot, and G. Nolet (2014). Automatic recognition of *T* and teleseismic *P* waves by statistical analysis of their spectra: An application to continuous records of moored hydrophones, *J. Geophys. Res.* **119,** no. 8, 6469–6485, doi: 10.1002/2013JB010936.

Sukhovich, A., J.-O. Irisson, F. J. Simons, A. Ogé, Y. M. Hello, A. Deschamps, and G. Nolet (2011). Automatic discrimination of underwater acoustic signals generated by teleseismic *P*-waves: A probabilistic approach, *Geophys. Res. Lett.* **38,** no. 18, L18605, doi: 10.1029/2011GL048474.

Talandier, J., and E. A. Okal (1998). On the mechanism of conversion of seismic waves to and from *T* waves in the vicinity of island shores, *Bull. Seismol. Soc. Am.* **88,** no. 2, 621–632.

Talandier, J., and E. A. Okal (2001). Identification criteria for sources of *T* waves recorded in French Polynesia, in *Monitoring the Comprehensive Nuclear-Test-Ban Treaty: Hydroacoustics*, C. deGroot Hedlin and J. Orcutt (Editors), Vol. 158, Birkhäuser Verlag, Basel, Switzerland, 567–603, doi: 10.1007/978-3-0348-8270-5_7.

Tanimoto, T. (2005). The oceanic excitation hypothesis for the continuous oscillations of the Earth, *Geophys. J. Int.* **160,** no. 1, 276–288, doi: 10.1111/j.1365-246X.2004.02484.x.

Tepp, G., and R. P. Dziak (2021). The seismo-acoustics of submarine volcanic eruptions, *J. Geophys. Res.* **126,** no. 4, e20912, doi: 10.1029/2020JB020912.

Wallace, L. M., S. C. Webb, Y. Ito, K. Mochizuki, R. Hino, S. Henrys, S. Y. Schwartz, and A. F. Sheehan (2016). Slow slip near the trench at the Hikurangi subduction zone, New Zealand, *Science* **352,** no. 6286, 701–704, doi: 10.1126/science.aaf2349.

Weatherall, P., K. M. Marks, M. Jakobsson, T. Schmitt, S. Tani, J. E. Arndt, M. Rovere, D. Chayes, V. Ferrini, and R. Wigley (2015). A new digital bathymetric model of the world's oceans, *Earth Space Sci.* **2,** 331–345, doi: 10.1002/2015EA000107.

Webb, S. C. (1998). Broadband seismology and noise under the ocean, *Rev. Geophys.* **36,** no. 1, 105–142, doi: 10.1029/97RG02287.

Wu, W., Z. Zhan, S. Peng, S. Ni, and J. Callies (2020). Seismic ocean thermometry, *Science* **369,** no. 6510, 151–115, doi: 10.1126/science.abb9519.

Manuscript received 24 February 2021
Published online 30 June 2021